AIAA JOURNAL
Vol. 45, No. 3, March 2007

Reacting and Nonreacting Flowfields of a V-Gutter Stabilized Flame

Scott M. Bush* and Ephraim J. Gutmark†
University of Cincinnati, Cincinnati, Ohio 45221

DOI: 10.2514/1.22655

Particle image velocimetry measurements have been performed to determine the flowfield around a confined V-gutter bluff body in both nonreacting and reacting environments. The incoming flow to the V-gutter bluff body is a vitiated mixture with secondary liquid fuel being injected upstream through a fuel spray bar to mimic realistic conditions. The measurements capture instantaneous and mean flow structures formed in the wake region of a three-dimensional bluff body. In addition to the flow structures, the mean velocity components, mean out-of-plane vorticity, and the turbulent kinetic energy have been compared between the nonreacting and reacting test cases. The results show significant differences in the instantaneous flow structures. The nonreacting case results in asymmetric shedding of large-scale vortical structures which span the entire wake region, whereas the reacting case results in both symmetric and asymmetric shedding of smaller scale vortical structures which are flattened out within the shear layer. A comparison of the mean velocity components clearly shows that the reacting case results in a larger region of reversed flow, experiences an acceleration of the freestream flow due to combustion, and results in a slower dissipation of the wake region.

Nomenclature

D	=	V-gutter width
Lrz	=	axial length of the recirculation zone
P_s	=	static pressure
T	=	mean local temperature
T_{rms}	=	root mean square of local temperature
T_b	=	bulk temperature
TKE	=	turbulent kinetic energy, $TKE = \frac{1}{2}(\overline{v_x'^2} + \overline{v_y'^2} + \overline{v_z'^2})$
V_b	=	bulk velocity, $V_b = \dot{m}/\rho_b A$
V_x, V_y, V_z	=	mean streamwise, transverse, and spanwise velocity components
$V_{X\text{rms}}$	=	root mean square of streamwise velocity component
v_x', v_y', v_z'	=	fluctuating streamwise, transverse, and spanwise velocity components
ρ_b	=	local bulk density
Φ	=	equivalence ratio
ω_z	=	vorticity about the z axis

Introduction

BLUFF bodies placed in combustible high-speed flows are used to stabilize flames. Typical applications for bluff-body stabilized flames include turbojet or turbofan afterburners in military aircraft, ramjet engines, and rocket motors. Bluff bodies stabilize flames by creating a large recirculation zone immediately downstream of the flame holding device. This recirculation zone consists of high-temperature burnt products that act as a continuous ignition source for the fresh fuel/air mixture. A considerable amount of research has been conducted on bluff-body stabilization, and comprehensive reviews of this topic can be found in [1–5].

More recent research has investigated the flowfield around a bluff body in both the nonreacting and reacting environments. These studies focused on the characterization of the velocity field, turbulence, flow structures, temperature field, and species present in the wake region of the bluff body. The jet engine manufacturer, Volvo Flygmotor AB, has carried out an extensive experimental study [6–8] to gain insight into this complex, dynamic flow environment and to aid in the validation of computational fluid dynamics codes. All of their experimental measurements were done with nonintrusive laser diagnostic techniques such as laser Doppler anemometry (LDA) and coherent anti-Stokes Raman scattering. They reported doubling of the recirculation zone for reacting conditions compared with nonreacting conditions and that strong vortex shedding is present in the nonreacting flow, but absent in the reacting flow. Similar experimental studies were performed by Fujii and Eguchi [9], Sanquer et al. [10], and Bakrozis et al. [11] who measured mean and turbulent velocities in both nonreacting and reacting wakes with LDA. Fujii and Eguchi [9] determined that turbulence is suppressed by combustion and that there is no vortex shedding in the reacting case. Sanquer et al. [10] compared probability density functions (PDFs) and frequency spectra in the wake region of various flame holders. They reported distinct changes in the statistical properties of the wake when combustion was occurring. The reacting wake had no vortex shedding, but for higher equivalence ratios longitudinal fluctuations in the flame front were captured in the spectra of the streamwise velocity component. A study performed by Yue et al. [12] uses particle image velocimetry (PIV) to study the flow structures present in the near-wake of a bluff body in a nonreacting environment. They showed that an asymmetric shedding of large-scale vortices is present in the near-wake region. Using the same setup as the experimental work done by Volvo Flygmotor AB, large eddy simulations (LES) coupled with subgrid scale models [13,14], Reynolds averaged Navier–Stokes [14], and a level-set flamelet library approach [15] were performed. These computational studies showed good agreement with the experimental results and validated their method of studying turbulent reacting flows. Furbey's computational study [13] correctly determined multiple combustion instability modes that were observed in the Volvo Flygmotor experimental tests.

Most of the previous experimental investigations have looked at the statistical properties of the flow, obtained with single-point measurement techniques such as LDA. These techniques make it

Presented as Paper 0807 at the 44th AIAA Aerospace Sciences Meeting and Exhibit, Reno, NV, 9–12 January 2006; received 23 January 2006; revision received 16 August 2006; accepted for publication 4 November 2006. Copyright © 2006 by Scott Bush. Published by the American Institute of Aeronautics and Astronautics, Inc., with permission. Copies of this paper may be made for personal or internal use, on condition that the copier pay the $10.00 per-copy fee to the Copyright Clearance Center, Inc., 222 Rosewood Drive, Danvers, MA 01923; include the code 0001-1452/07 $10.00 in correspondence with the CCC.

*Ph.D. Student, Department of Aerospace Engineering and Engineering Mechanics, 745 Baldwin Hall. Student Member AIAA.

†Professor and Ohio Eminent Scholar, Department of Aerospace Engineering and Engineering Mechanics, 745 Baldwin Hall. Associate Fellow AIAA.

difficult to investigate the flow structures and flow dynamics associated with unsteady complex flowfields such as bluff bodies. Flow visualization techniques provide insight into the flow structures, but they only offer qualitative information about the flow and can be inconclusive. The use of quantitative, multipoint measurement techniques such as PIV are well suited to study instantaneous flow structures and flow dynamics of complex turbulent nonreacting and reacting flows. A study performed by Ji and Gore [16] demonstrates the PIV measurement technique within a complex swirling flow with and without combustion, in which they were able to accurately capture the mean and instantaneous flow structures.

In the present investigation, the flowfield downstream of a confined V-gutter bluff body in both nonreacting and reacting conditions is described. This study contributes to the current literature by detailing the differences in the instantaneous flow structures and vorticity fields associated with the nonreacting and reacting conditions. Also, the facility uses an upstream preburner to accurately simulate the flow environment encountered within a jet engine afterburner. The incoming flow to the V-gutter bluff body is a vitiated mixture with secondary liquid fuel being injected upstream through a fuel spray bar to mimic realistic conditions. The V-gutter geometry used in this study is also different than any previous studies. PIV is used to capture instantaneous and mean flow structures formed in the wake of a three-dimensional bluff body. In addition to the flow structures, the mean velocity components, mean out-of-plane vorticity, and the turbulent kinetic energy are compared in nonreacting and reacting test cases.

Experimental Setup and Methods

Afterburner Simulation Facility

The experimental investigations were conducted in the afterburner simulation facility (ABSF) shown in Fig. 1. The operating parameter ranges for the ABSF are listed in Table 1. The test rig includes a premixed can combustor from a GE J-73 turbojet engine. The premixed can combustor is operated on a mixture of air and Jet A fuel. Both the incoming air and Jet A fuel are initially at room temperature. The combustion products from this burner pass through a flow conditioning screen and then enter a section that transitions the cross section of the duct from a 177.8 mm circular pipe to a 152.4 mm square duct followed by a converging nozzle that terminates in a 152.4×76.2 mm constant area duct. This duct consists of an inlet section (length, 228.6 mm), test section (length, 596.9 mm), and exhaust section (length, 228.6 mm). The inlet and exhaust sections are instrumented with type K thermocouples (± 2.2 K) and static pressure transducers (Druck PMP 4065, $\pm 0.08\%$ full-scale accuracy, 68.95 kPa range) to measure the temperature and pressure of the flow before and after the test section. The inlet section also houses a fuel spray bar 254 mm upstream of the V-gutter. The fuel spray bar is a hollow cylinder with ten 0.457-mm-diam holes spaced 12.7 mm apart spanning the facility from the bottom wall to the top wall and centered on the same axis as the V-gutter, as shown in Fig. 1. The injection occurs from five holes on both sides of the bar perpendicular to the flow. Jet A fuel is used for all of the V-gutter testing and is mixed with the incoming vitiated flow from the upstream preburner. The test section is of a modular design with interchangeable walls to allow for the use of different types of instrumentation. The test sections top wall and side walls can be replaced with quartz window inserts (101.6×139.7 mm, 254×139.7 mm, 101.6×63.5 mm, 254×63.5 mm) to allow for optical access and the use of advanced laser diagnostics. The outlet of the constant area duct ends in an expansion to a 254 mm circular duct.

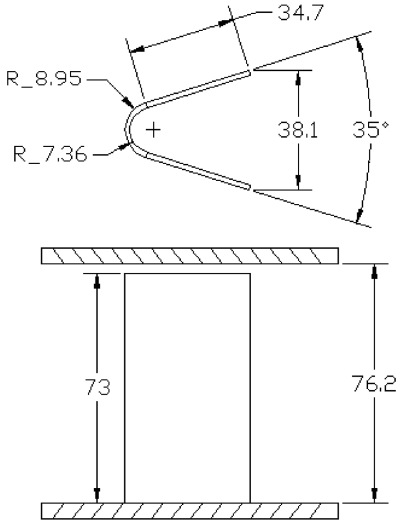

Fig. 2 Schematic of the V-gutter flame holder (units in millimeters).

The V-gutter used in this study is made from 15.9-mm-thick Hastelloy X and is shown in Fig. 2 along with its dimensions. The V-gutter width is 38.1 mm and has a spread angle of 35 deg. The V-gutter does not span the entire 76.2 mm duct with its height being only 73 mm to allow for thermal expansion. Using the coefficient of thermal expansion for Hastelloy X, the V-gutter may experience a maximum growth of 1.2 mm at a material temperature of 1255 K. This small clearance gap allows for the crossflow to leak over the top of the V-gutter creating a three-dimensional flowfield in the wake of the flame holder.

As shown in Table 1, the ABSF has a range of conditions at which it can operate. Therefore, a particular set of conditions were chosen to perform the required tests and these conditions are listed in Table 2. The incoming bulk velocity was computed using a local bulk density that was determined within the inlet section from a bulk temperature and static pressure. The tests were performed by igniting the GE J-73 preburner and setting a specific bulk velocity and bulk temperature of the incoming flow in the facility. The pressure of the facility remained near atmospheric conditions. The two test cases performed in this study were completed with the same inlet bulk velocity, bulk temperature, and pressure. Case 1 was completed with isothermal conditions and case 2 was completed with a stabilized flame behind the V-gutter.

Particle Image Velocimetry

The tracer particles used to seed the flow in performing the PIV studies were 5 μm Al_2O_3. These particles closely follow the reacting flow and were illuminated by a New Wave Research double-pulsed Nd:YAG PIV laser. The laser output power is 120 mJ/pulse at a repetition frequency of 15 Hz and a wavelength of 532 nm. An appropriate combination of cylindrical lenses generates a light sheet that illuminates a two-dimensional plane of the flow in the test

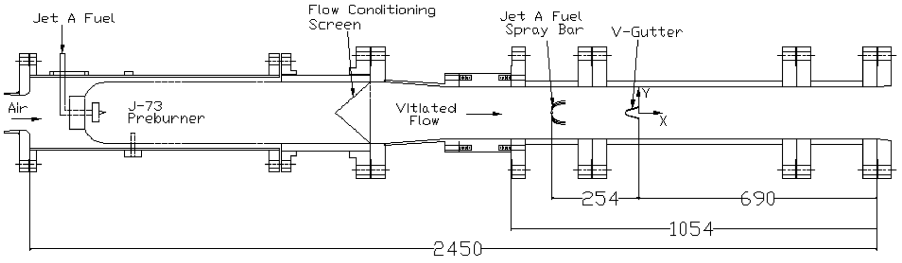

Fig. 1 Schematic of the afterburner simulation facility (units in millimeters).

Table 1 Afterburner simulation facility operating conditions

Operating parameter	Ranges
Inlet stagnation pressure	103.4–110.3 kPa
Inlet stagnation temperature	290–930 K
Air mass flow rate	up to 0.816 kg/s
Total/static pressure ratio	up to 1.064
Inlet Mach number	up to 0.30

Table 2 Summary of test conditions

Cases	V_b, m/s	T_b, K	P_s, kPa	Φ
1	53.3	644.3	101.3	0
2	53.3	644.3	101.3	0.41

section. The illuminated tracer particles are captured by a LaVision couple-charged digital (CCD) camera. The camera resolution is 1376×1040 pixels with each pixel being 6.45×6.45 μm. A 50 mm/f1.4 Nikon lens and a 532 nm narrow bandpass filter are used for all cases tested.

The raw data is processed into velocity data on a dual Pentium 4 processor with 1 GB RAM used to control the data acquisition. Each raw PIV image is divided into a constant size 64×64 pixel interrogation window with a resulting spatial resolution of 3×3 mm. The velocity vectors are calculated by a cross-correlation technique with 50% overlapping and a standard fast Fourier transform (FFT) algorithm performed between the two frames of the raw PIV data. In each test case, data sets of 250 raw PIV images were acquired. The uncertainty associated with the PIV processing technique has been investigated by McKenna and McGillis [17] for different cross-correlation techniques and determines the effect on uncertainty for varying interrogation window sizes. They determined that error decreases with increasing interrogation window size. A 32×32 pixel interrogation window with a FFT cross-correlation algorithm results in an error of 1.93% in the velocity computations and an error of 2.39% for the vorticity [17]. The current study uses a larger interrogation window size and therefore the uncertainty associated with the processing will be less than the aforementioned values. The uncertainty associated with the calibration is estimated to be less than 1%. The overall error in the velocity data is estimated to be around 2.5% and the error in the vorticity calculations is estimated around 3%. Ji and Gore [16] report a similar uncertainty in their PIV analysis and also discuss the thermophoretic forces experienced by the seeding particles in reacting environments. They report that these forces are negligible in strongly swirling flows based on a study completed by Sung et al. [18] that concluded that the forces were negligible in high-speed flows. The present study has a high-speed flow and therefore the thermophoretic forces are assumed negligible in this investigation.

PIV measurements are taken at multiple x–y planes in the V-gutter wake, as shown in Fig. 3. All images acquired in the x–y plane are captured along the centerline of the tunnel at $z = 39.1$ mm. Measurements in the x–z plane are taken at a single location in the near field of the V-gutter wake as shown in Fig. 3. The images in the x–z plane are acquired along the centerline of the tunnel at $y = 0$.

Results and Discussion

Upstream Boundary Conditions

Initial measurements were performed $6.67D$ upstream of the V-gutter flame holder to characterize the incoming flow properties. Figure 4 shows the mean and rms velocity and temperature profiles that were determined in the transverse and spanwise directions along the centerlines of the facility at $z = 38.1$ mm and $y = 0$ mm. Along both centerlines of the facility, the mean and rms streamwise velocity profiles have similar characteristics to a fully developed turbulent duct flow. The upstream preburner and flow conditioning screen thoroughly mix the combustion exhaust products resulting in a parabolic-shaped temperature profile. Figure 4a shows the mean temperature profile in the transverse direction has a peak along the centerline of the facility with a steady drop off in temperature as the walls of the inlet section are approached. Figure 4b shows that the mean temperature profile again has a peak along the centerline of the facility, but a more uniform distribution is achieved in the spanwise direction as a result of the upstream contoured nozzle. The rms temperature profiles follow a similar trend in both directions with a maximum along the centerline and a gradual decrease in fluctuation as the walls are approached.

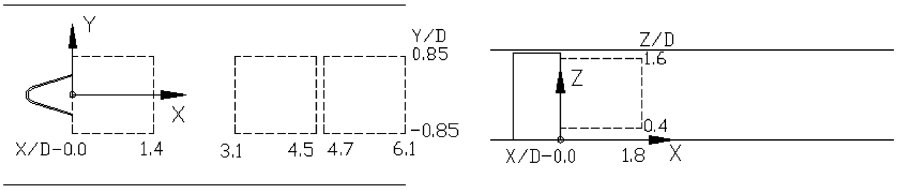

Fig. 3 PIV measurement regions for various planes in the V-gutter wake.

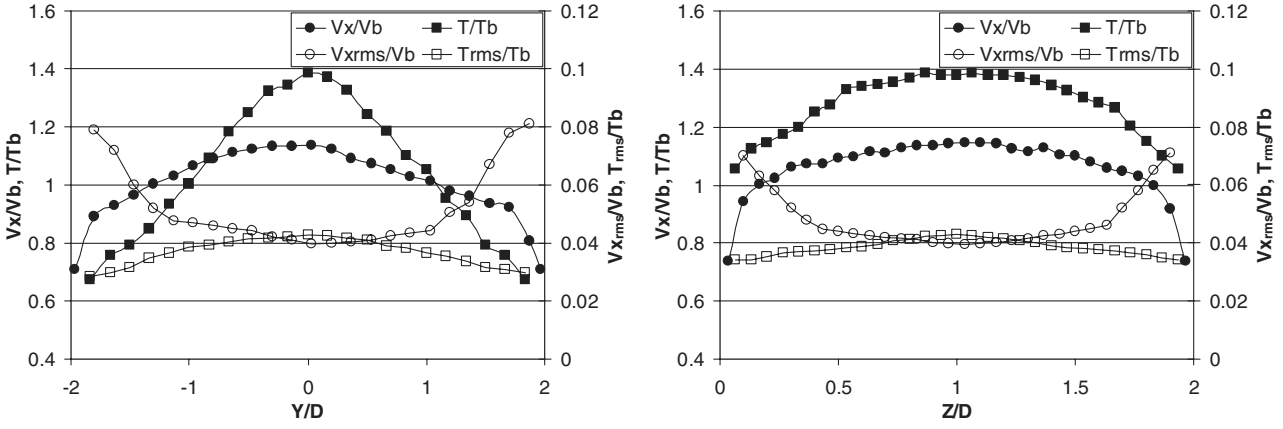

a) Transverse centerline **b) Spanwise centerline**

Fig. 4 Mean and rms velocity and temperature profiles.

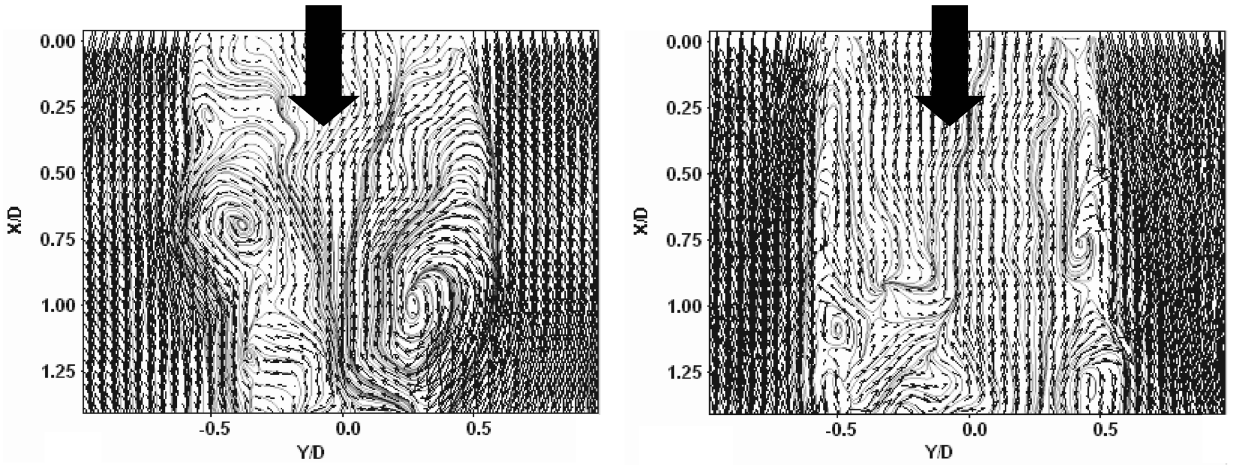

a) Nonreacting b) Reacting

Fig. 5 Instantaneous flow structures for different conditions.

PIV Measurements in the *x–y* Plane

Flowfield Structures

Measurements in the x–y plane of the instantaneous flow structures show significant differences in nonreacting conditions compared with reacting conditions. Figure 5 compares a typical instantaneous velocity vector field formed in the near-wake region behind the bluff body for the different conditions. The incoming flow is from top to bottom with the end on the V-gutter located at $X/D = 0$. The nonreacting case results in asymmetric shedding of large-scale vortices from the V-gutter edges, as has also been found experimentally [7] and numerically [13,14]. The reacting case results in smaller scale elongated vortical structures that are confined within the shear layer. Both symmetric and asymmetric shedding of vortices is observed. Prior observations for different inlet conditions have also shown both symmetric and asymmetric shedding for reacting conditions behind a bluff body [14].

To investigate the mean structures present within the flowfield, the 250 instantaneous velocity vector fields were averaged. Figure 6 represents the mean velocity vector fields for the two cases tested as well as the mean flame location for the reacting test case. The major distinction from the instantaneous velocity field is that time-averaged vortical structures are now symmetric about the centerline. The symmetry occurs in the time-averaged velocity field because the instantaneous images are taken at random time intervals. The random time interval allows for the asymmetric structures to be at different locations within the various instantaneous images. With a large number of random instantaneous images, the time-averaged image will result in two symmetric low-velocity regions. Figure 6a and 6b clearly represent the two symmetric low-velocity regions that are commonly reported for time-averaged bluff-body flows. The main difference between the nonreacting and reacting condition is the size and location of these symmetric low-velocity regions. For the nonreacting case shown in Fig. 6a, the center, where the absolute velocity is zero, of the low-velocity regions is located at a downstream distance near $X/D = 0.80$. For the reacting case shown in Fig. 6b, the center of the low-velocity regions has clearly moved further downstream near a location of $X/D = 1.25$. In addition to the center moving further downstream for the reacting case, the overall shape of the mean large-scale structure has been elongated and confined to the shear layer compared with the nonreacting test case. Figure 6b also shows the mean flame boundaries in relation to the mean velocity vector field for the reacting test case. The flame boundaries are obtained by taking a raw image of the stabilized flame with a CCD camera. The flame is located on both sides of the V-gutter and extends from the tips of the V-gutter downstream in the shear layers created by the bluff body. In the shear layers, strong mixing occurs between the fresh unburnt mixture and the hot burnt gases due to the vortex shedding. The flame is initially very thin near the tips of the V-gutter and grows in thickness as it extends further downstream. The outer boundaries of the flame spread slowly and are a function of the local flow velocity and the turbulent flame speed.

To further quantify the differences in the instantaneous flow structures occurring in nonreacting and reacting environments, probability density functions have been formulated to compare the statistical properties of the velocity components. Figure 7 displays the PDFs of the transverse, V_y/V_b, and streamwise, V_x/V_b, velocity

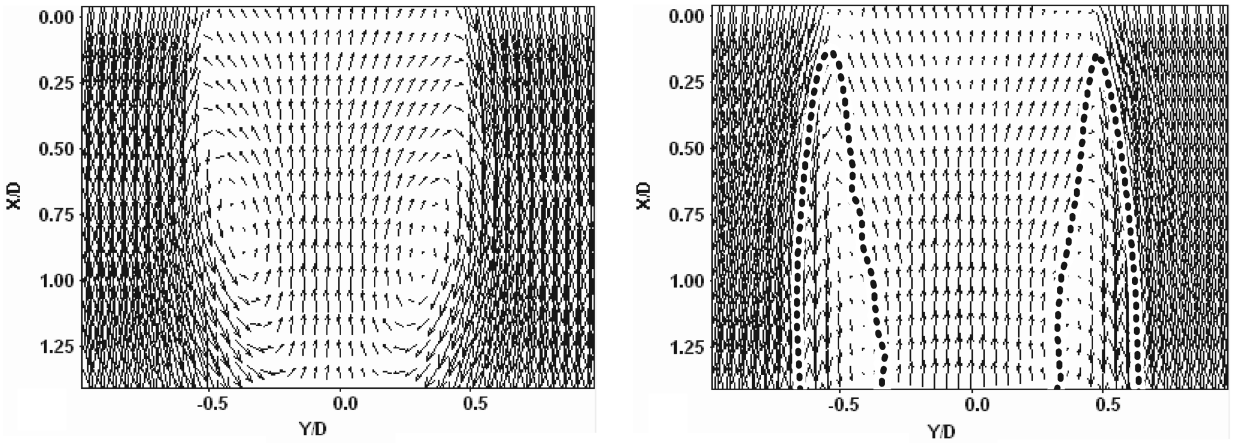

a) Nonreacting b) Reacting

Fig. 6 Mean velocity vector plots for different conditions with flame boundaries.

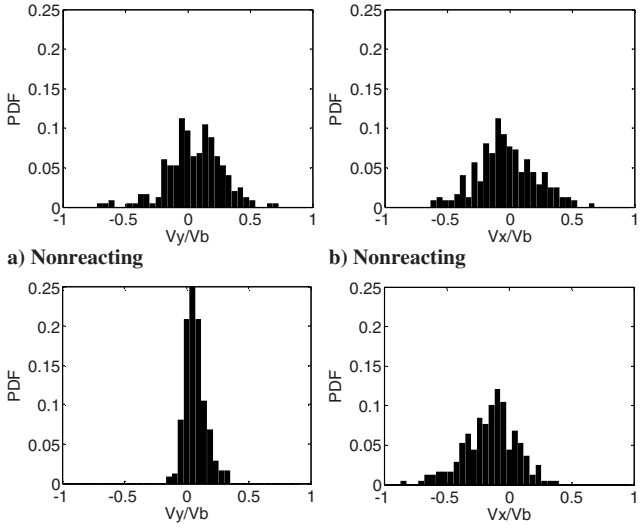

Fig. 7 PDFs of the transverse V_y and streamwise V_x velocity components.

components for nonreacting and reacting conditions. The PDFs were determined within the shear layer at the location where the nonreacting time-averaged absolute velocity was zero corresponding to $X/D = 0.8$ and $Y/D = 0.4$. The main difference that can be observed from the PDFs is in the transverse velocity component. For the nonreacting case, the transverse velocity component (Fig. 7a) is spread about zero with peaks on both sides of zero. This is explained by the large-scale vortical structures being shed from the V-gutter edge and the random time interval of the instantaneous images. At different instances in time, the vortical structures are captured in different locations downstream of the V-gutter. If the large structure is past the measurement point, then a positive transverse velocity is obtained and the opposite is true if the structure has not reached the measurement point. For the reacting case, the transverse velocity component (Fig. 7c) has a single narrow peak near zero. This occurs because the vortical structures are much smaller in size and maintained within the shear layer. The statistical analysis helps conclude that large-scale vortical structures are being shed for the nonreacting case and smaller scale vortical structures are being shed for the reacting case.

Mean Streamwise Velocity Distributions

With distinct differences being observed in the flow structures of nonreacting and reacting flowfields, further comparison of the velocity flowfield is carried out by analyzing the mean velocity components within the flow. Figure 8 compares the nondimensional mean streamwise velocity component, V_x/V_b, of both nonreacting and reacting conditions at two downstream measurement planes. Figures 8a and 8c show the near-field plane downstream of the bluff body where the recirculation zone is present. All negative velocities measured within the recirculation zone are represented with dashed contour lines and all positive velocities are represented with solid contour lines. Comparing the isothermal case shown in Fig. 8a to the reacting case shown in Fig. 8c, some distinct differences are observed. The magnitude of the negative streamwise velocities within the recirculation region is greater in the reacting case and is also shifted further downstream than the nonreacting case. The contour lines within the shear layer spread more rapidly in the nonreacting case with increases in downstream distance representing a quicker dissipation of momentum within the wake region. The freestream fluid for both cases goes through the same acceleration around the V-gutter, but the effects of combustion in the reacting case results in further acceleration of the freestream fluid due to decreases in the fluid density and maintaining the same mass flow rate. Figures 8b and 8d represent a measurement plane further downstream for the nonreacting and reacting cases, respectively.

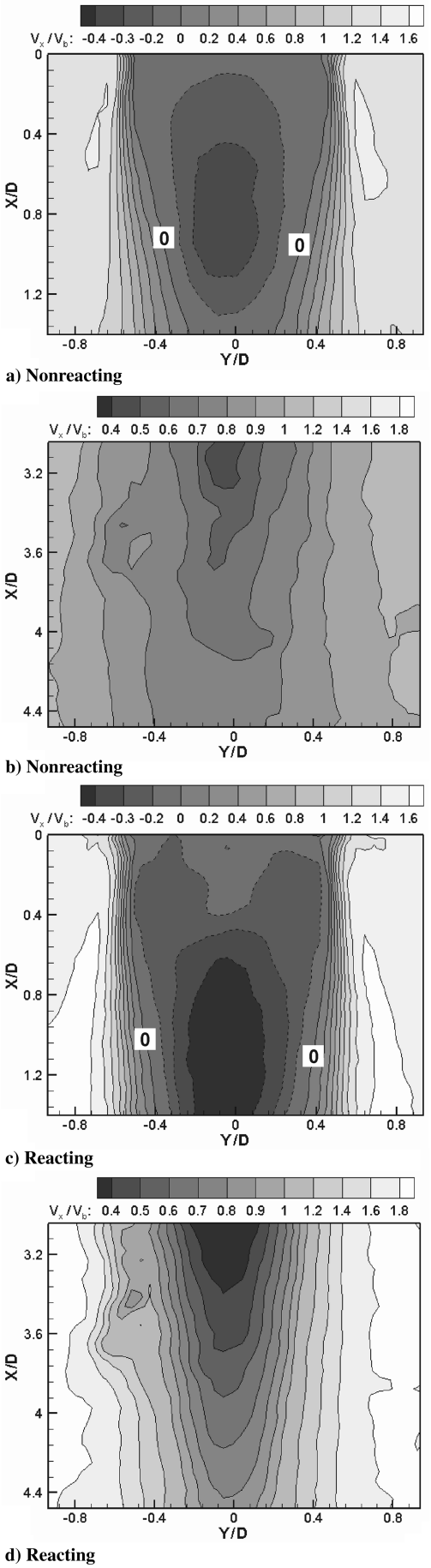

Fig. 8 Mean contour plots of the streamwise velocity (notice contour scale value differences).

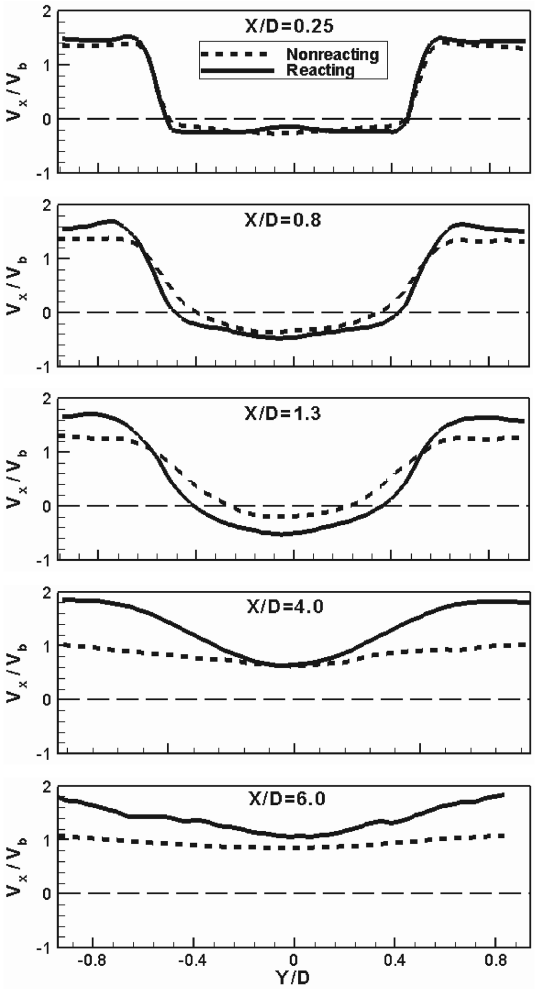

Fig. 9 Profiles of the streamwise velocity at various X/D locations in three x–y plane regions.

These results show similar trends to the near-field plane in that the contour lines are spread further apart for the nonreacting case with the wake region approaching a uniform velocity distribution. For the reacting case, the wake region is still easily identifiable and the freestream fluid has continued to accelerate in the downstream direction.

The variation of the streamwise velocity at various downstream distances is represented in Fig. 9 by line profiles. These line profiles allow for a direct comparison of the nonreacting and reacting cases at five different locations downstream of the V-gutter. Just downstream of the V-gutter at $X/D = 0.25$, the nonreacting and reacting cases are nearly identical. Differences become noticeable at the other four locations measured downstream of the bluff body. The comparison clearly shows that the reacting case has a larger region of reversed flow, an acceleration of the freestream flow due to combustion, and a slower dissipation of the wake region which was also observed by Sjunnesson et al. [7]. Comparison of the streamwise velocity component along the centerline of the V-gutter for both nonreacting and reacting conditions with Sjunnesson et al. [7] and Fujii and Eguchi [9], is shown in Fig. 10. The results show similar trends in the flow characteristics observed by Fujii and Eguchi [9] and Sjunnesson et al. [7], however, the differences in values may be attributed to different experimental setups. Both of the prior studies [7,9] used flame holders with an equilateral triangle cross section spanning the entire width of the test section resulting in a two-dimensional bluff body, whereas the current study examines a 35 deg spread angle V-gutter flame holder with a small clearance gap creating a three-dimensional bluff body. Sjunnesson et al. [7] tested an equilateral triangle with a side length of 40 mm spanning a 240 × 120 mm test section, whereas Fujii and Eguchi [9] studied an equilateral triangle having a side length of 25 mm spanning a 50 × 50 mm test section.

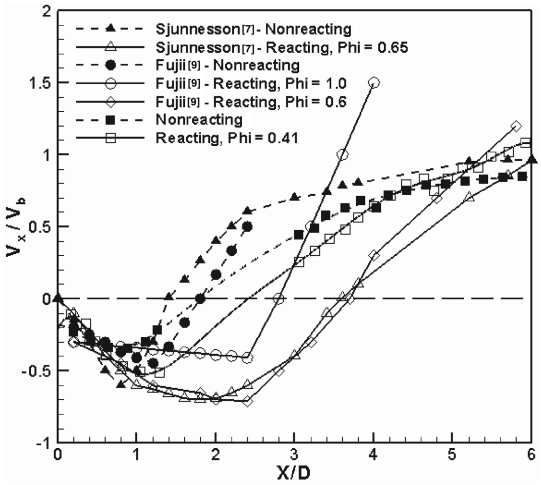

Fig. 10 Centerline profiles at $Y/D = 0$ of the streamwise velocity.

For the current study, the measured streamwise velocities are represented by the symbols in the plot and a trend line was passed through these points to allow for extrapolation in the regions with no data. All three studies result in a shorter recirculation zone for the isothermal case and Fujii and Eguchi [9] show the effect of equivalence ratio on the recirculation zone length. As well, the velocities in the isothermal cases are approaching a nondimensional value of one and the reacting cases show the wake region continuing to accelerate due to combustion.

Mean Transverse Velocity Distributions

Figure 11 compares the nondimensional mean transverse velocity component, V_y/V_b, for the nonreacting and reacting conditions at two downstream planes. The two planes shown are the same planes that were described in the preceding section. The dashed contour lines correspond to negative velocities whereas the solid contour lines represent positive velocities. Comparing the isothermal case shown in Fig. 11a to the reacting case shown in Fig. 11c, it is clear that differences are created by the combustion process. In the nonreacting case, the freestream flow is initially forced away from the V-gutter surface toward the tunnel walls as it accelerates around it. As the freestream flow continues downstream to near $X/D = 0.6$, it approaches zero transverse velocity where all the flow is in the streamwise direction and it then flows back inward toward the centerline of the V-gutter. The flow contained within the recirculation zone is flowing around the two low-velocity regions shown in Fig. 6a with the centerline transverse velocity being near zero. For the reacting case, the freestream flow is again forced away from the V-gutter surface toward the tunnel walls, but for this case the freestream continues to flow toward the tunnel walls rather than turning back inward toward the centerline of the V-gutter. The transverse velocity within the recirculation zone is similar to the nonreacting case in the upper half of the image. In the reacting case, the two low-velocity regions shown in Fig. 6b are further downstream causing the differences in the transverse velocities in the lower half of the image. Figures 11b and 11d represent a measurement plane further downstream for the nonreacting and reacting cases, respectively. In the nonreacting case, the mean transverse velocity is still flowing inwards toward the centerline of the bluff body, but on a much lower scale than the near-field plane. For the reacting case, the flow within the flame is moving toward the centerline of the V-gutter and approaching zero transverse velocity outside of the flame region.

To quantify and compare the variation of the transverse velocity for both nonreacting and reacting conditions, line profiles at various downstream distances is represented in Fig. 12. At $X/D = 0.25$, it is clear that for both cases the freestream flow is being pushed away from the V-gutter surface toward the tunnel walls. A noticeable difference is observed in the reacting case with a peak in transverse

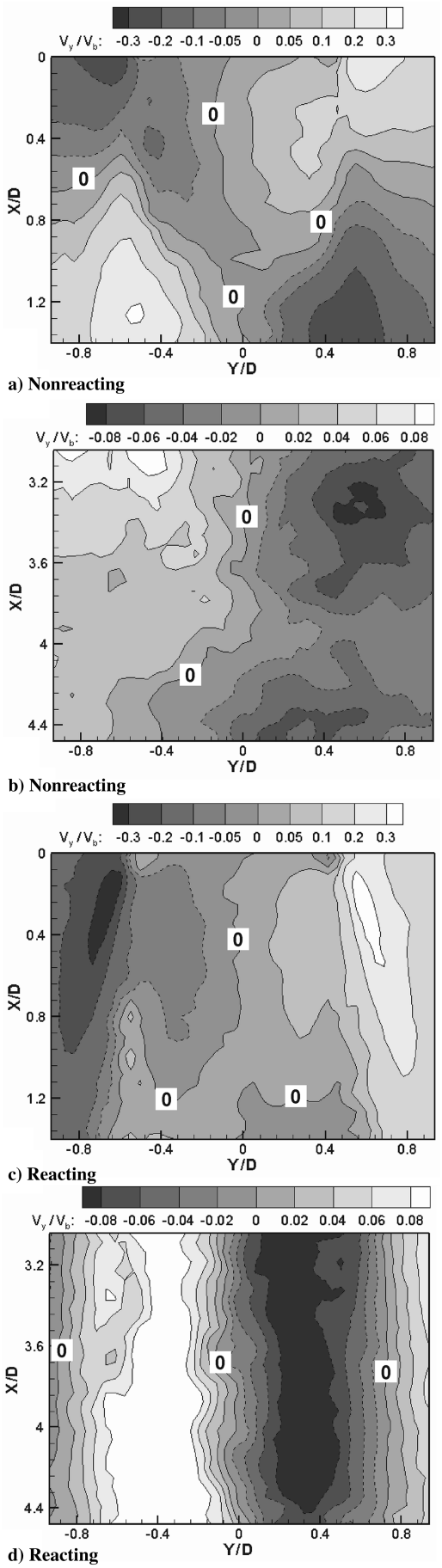

Fig. 11 Mean contour plots of the transverse velocity (notice contour scale value differences).

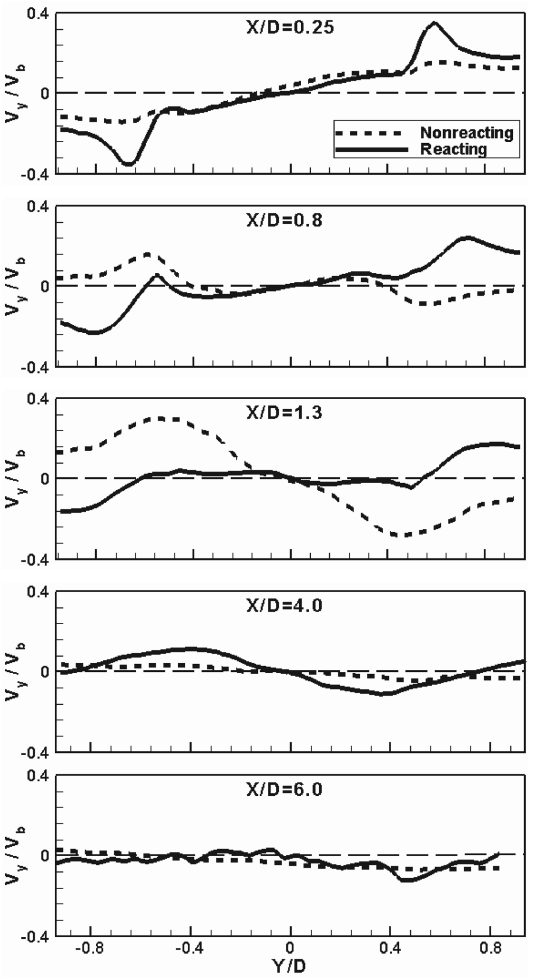

Fig. 12 Profiles of the transverse velocity at various X/D locations in three x–y plane regions.

velocity just on the outer edge of the stabilized flame. This particular peak in transverse velocity was also observed in reacting bluff-body flows by Sjunnesson et al. [7] and Fujii and Eguchi [9]. At $X/D = 0.8$ and 1.3, the nonreacting freestream has now flipped across the zero axis, meaning the flow is now heading inward toward the centerline of the V-gutter. The reacting case remained in a similar location, meaning that the freestream flow is still moving toward the tunnel walls. At $X/D = 4$, the reacting case has flipped across the zero axis within the flame region, meaning it is now flowing toward the V-gutter centerline and is approaching zero transverse velocity outside the flame boundaries. For the nonreacting case, the flow is nearly all in the streamwise direction and at $X/D = 6$, both cases are almost all in the streamwise direction.

Mean Vorticity and Turbulent Kinetic Energy

The mean out-of-plane vorticity in the x–y plane is determined by Eq. (1). A comparison of the nondimensional mean out-of-plane vorticity, $\omega_z D/V_b$, for the nonreacting and reacting cases

$$\omega_z = \partial V_x/\partial y - \partial V_y/\partial x \tag{1}$$

is shown in Fig. 13. For both the nonreacting and reacting cases, the shear layer created around the recirculation zone is clearly depicted by the concentration of negative and positive vorticity contours that originate from opposite edges of the V-gutter. The maximum vorticity occurs within the shear layer just downstream of the V-gutter tips. In both cases, the vorticity distribution is initially closely spaced and spreads out with downstream distance as it loses strength. For the nonreacting case shown in Fig. 13a, the vorticity begins to bend inward toward the centerline of the V-gutter representing the

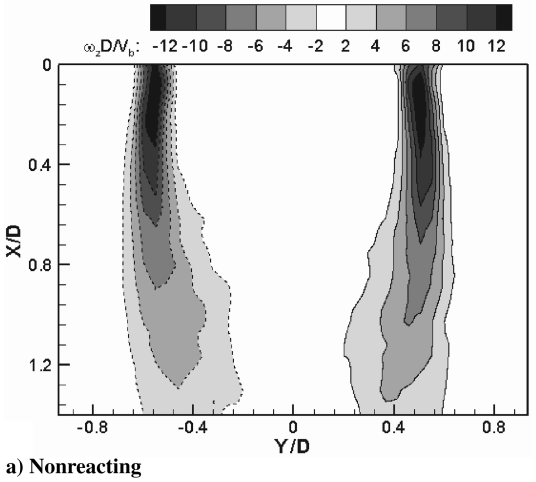

a) Nonreacting

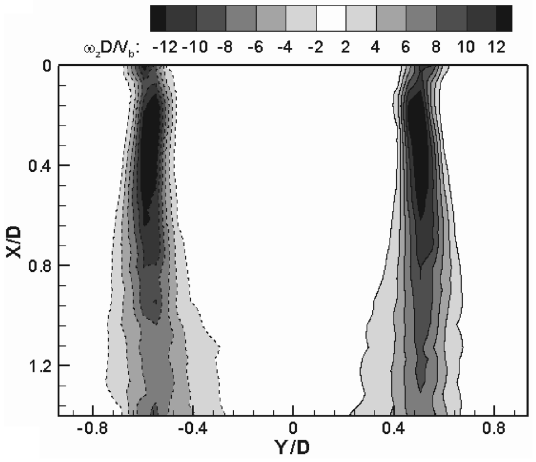

b) Reacting

Fig. 13 Mean contour plots of vorticity about the z axis for different conditions.

end of the recirculation region. Comparing these results to the reacting case shown in Fig. 13b, it can be seen that the vorticity maintains its strength further downstream and does not begin to bend inward. This is in agreement with earlier results that the reacting case has a longer recirculation zone and therefore the vorticity is not bending inward toward the centerline until further downstream.

The variation of the nondimensional mean out-of-plane vorticity, $\omega_z D/V_b$, along the shear layer, $Y/D = 0.5$, is given in Fig. 14. In both cases, the maximum vorticity occurs just downstream of the V-gutter lip. The reacting case results in a slight increase in vorticity strength compared with the nonreacting case and has its maximum vorticity occurring further downstream than the nonreacting case. Both cases follow a similar decay in vorticity strength with increases in downstream distance and are approaching zero rotation within the flow. The nonreacting case has achieved nearly zero rotation within the flow at a downstream distance of $X/D = 4$, whereas the reacting case is still approaching zero at $X/D = 6$.

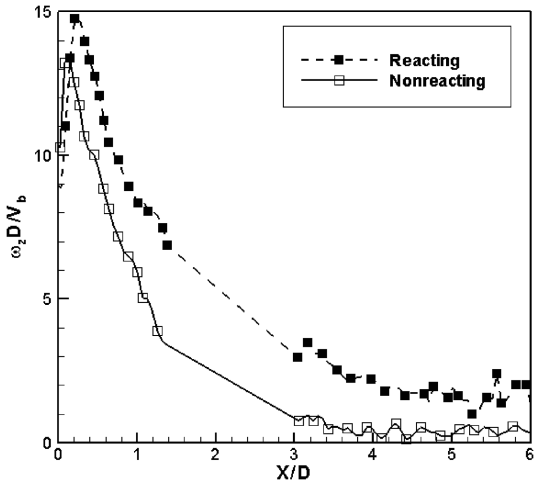

Fig. 14 Line profile of vorticity along the shear layer at $Y/D = 0.5$.

The turbulent kinetic energy is defined in Eq. (2) assuming isotropic turbulence [19], which was also assumed by Fujii and Eguchi [9] about the third fluctuating velocity component. This study is limited to two-dimensional data and therefore the third fluctuating component is taken as the average of the other two, resulting in the final form shown.

$$TKE = \frac{1}{2}(\overline{v_x'^2} + \overline{v_y'^2} + \overline{v_z'^2}) \quad \text{where } \overline{v_z'^2} = \frac{1}{2}(\overline{v_x'^2} + \overline{v_y'^2})$$
$$TKE = \frac{3}{4}(\overline{v_x'^2} + \overline{v_y'^2}) \tag{2}$$

The values for v_x' and v_y' are within 10% of each other for the majority of the x–y plane and v_z' is known for the x–z center plane which varies from the calculated value by a maximum of 15%. The uncertainty in the TKE values is estimated to have an error of around 15%. A comparison of the mean nondimensional turbulent kinetic energy, TKE/V_b^2, for the nonreacting and reacting cases is shown in Fig. 15. The turbulent kinetic energy gives insight into the vortical structures and the mixing processes involved in complex dynamic flows. For the nonreacting case shown in Fig. 15a, the mean TKE contours represent the path of the asymmetric large-scale vortical structures being shed from V-gutter edges and convected downstream while moving inward toward the V-gutter centerline. These large-scale

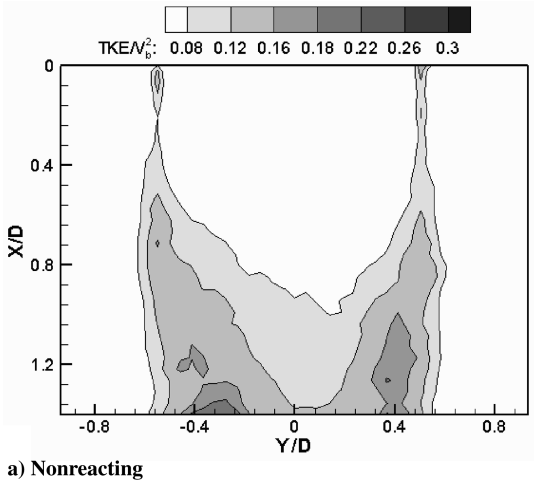

a) Nonreacting

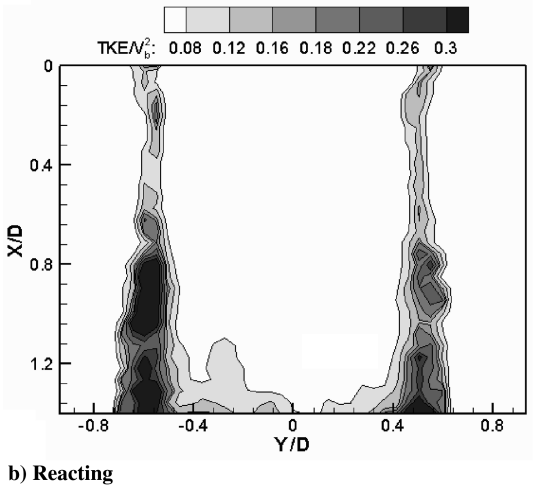

b) Reacting

Fig. 15 Mean contour plots of turbulent kinetic energy for the two cases.

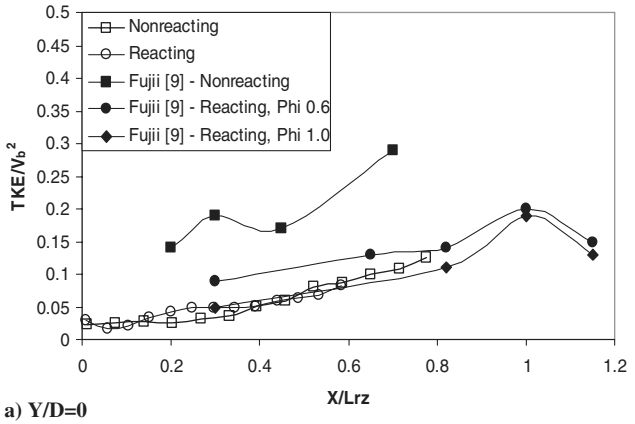

a) Y/D=0

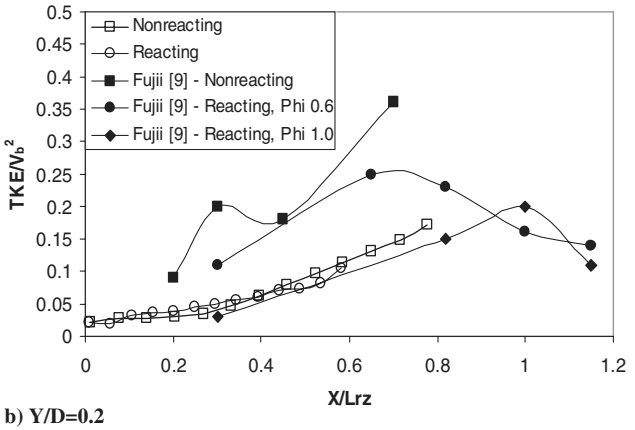

b) Y/D=0.2

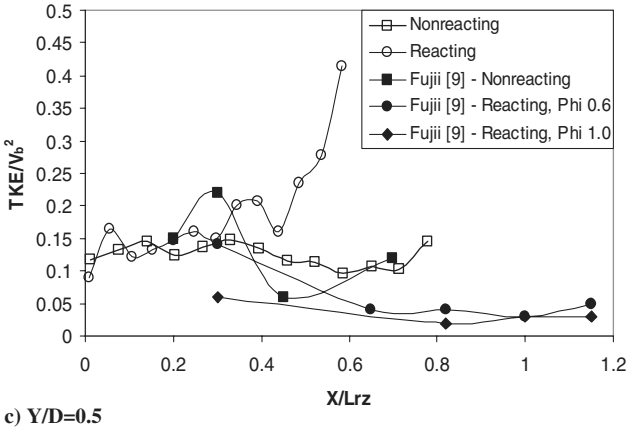

c) Y/D=0.5

Fig. 16 Line profiles of turbulent kinetic energy in the wake of the V-gutter.

structures promote intense mixing between the freestream fluid and the recirculating flow in the near-wake region of the bluff body. For the reacting case shown in Fig. 15b, the mean TKE contours are mainly located within the shear layer until a downstream distance of $X/D = 1.3$. This shows that the roll-up and shedding of the flattened smaller scale vortices is mainly occurring within the shear layer where the chemical reaction takes place. The vortex shedding within the shear layer promotes intense mixing between the fresh freestream mixture and the hot products of the recirculation zone as they are convected downstream.

Comparison of the turbulent kinetic energy levels behind the V-gutter for both nonreacting and reacting conditions with Fujii and Eguchi [9] is shown in Fig. 16. The downstream distance has been nondimensionalized with the axial length of the recirculation zone. Figures 16a and 16b show a collapsing of the TKE levels within the recirculation zone for the current study, however Fujii and Eguchi [9] measured higher levels of TKE for the nonreacting case in comparison to the reacting case. In the current study, TKE levels for the reacting case are in excellent agreement with the values measured by Fujii and Eguchi [9] for an equivalence ratio of one. Figure 16c compares the TKE levels within the shear layer and shows a large increase in TKE levels for the reacting case. This result differs from Fujii and Eguchi [9], as they report a drop in TKE levels for the reacting case. They attributed lower values of TKE to the destruction of turbulent kinetic energy due to the dilation associated with heat release. However, it was predicted by Bray and Libby [20] that production of turbulent kinetic energy within an oblique flame would compete with or dominate the dilation associated with heat release. This could explain the larger values of TKE observed within the shear layer for the reacting case.

PIV Measurements in *x–z* Plane

Measurements in the x–z plane were only made for the isothermal case. The x–z plane gives insight into the three-dimensional effects in the wake of the V-gutter due to the 3.2 mm gap near the top wall of the tunnel. Figure 17 shows the instantaneous and mean flow structures along the centerline of the V-gutter in the recirculation region just downstream of the bluff body. The freestream flow is from left to right with the V-gutter ending at $X/D = 0$. The instantaneous velocity field in Fig. 17a shows a large-scale vortical structure in the upper half of the recirculation zone due to the clearance gap near the top wall. Figure 17b represents the mean structures present within the flowfield by taking an average of the 250 instantaneous velocity vector fields. The time-averaged flowfield results in a large-scale vortical structure represented by the low-velocity region at a height of $Z/D = 1.3$. This shows that a large three-dimensional vortical structure is present in the near-wake region of the bluff body. This three-dimensional structure consists of the two symmetric vortical structures observed in Fig. 6a being shed from the edges of the V-gutter and the single vortical structure observed in Fig. 17b being created by the leakage of flow over the top of the bluff body. A similar three-dimensional large-scale vortical structure was observed in computational studies by Krajnovic and Davidson [21].

To further quantify the recirculation region, the mean velocity components are analyzed and shown in Fig. 18. Figure 18a represents the nondimensional mean streamwise velocity, V_x/V_b,

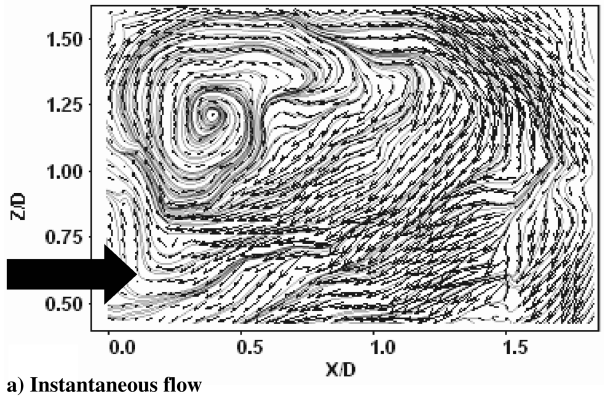

a) Instantaneous flow

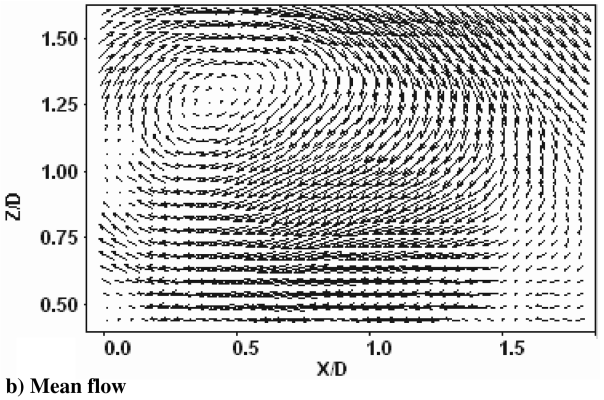

b) Mean flow

Fig. 17 Velocity vector plots for nonreacting conditions in the *x–z* plane.

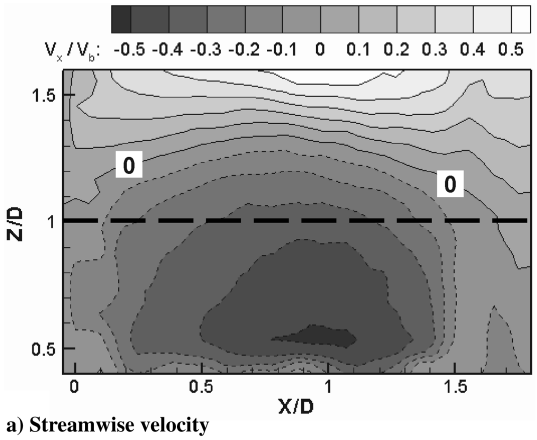

a) Streamwise velocity

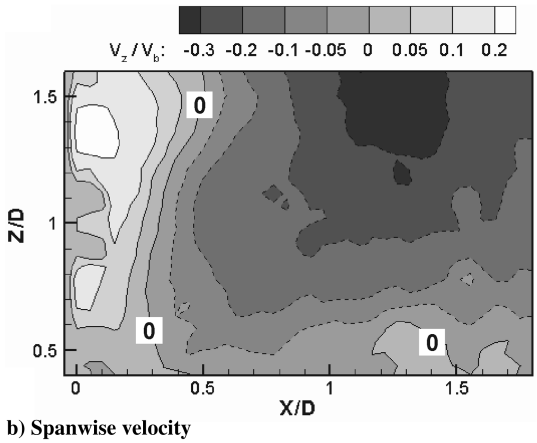

b) Spanwise velocity

Fig. 18 Mean contour plots of velocities in the *x–z* plane for nonreacting conditions.

and its variation across the height of the V-gutter. The line in Fig. 18a represents the height of the *x–y* measurement plane discussed in the preceding sections and has a nearly identical profile to the isothermal centerline profile in Fig. 10. The dashed contour lines again represent negative flow and the solid contour lines represent positive flow. The region of reversed flow does not span the entire tunnel height and is limited to the lower two-thirds of the tunnel height, by observing the location of the zero streamwise velocity contour. This gives insight into a recirculation bubble that would form behind this particular bluff body. The region of reversed flow would be from the bottom wall out to the edges of the V-gutter spanning up the V-gutter approximately two-thirds of the tunnel height and going back a distance $X/D = 1.7$. Figure 18b shows the variation of the nondimensional mean spanwise velocity, V_z/V_b, in the near-wake region. The spanwise velocity is flowing upward toward the top wall just downstream of the V-gutter edge and flows downward on the far side of the vortical structure centered at $Z/D = 1.3$ and $X/D = 0.4$.

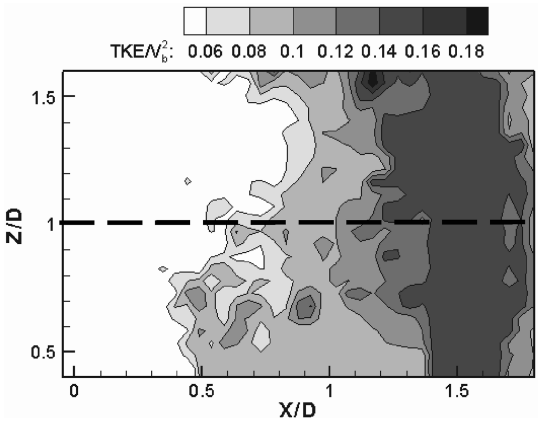

Fig. 19 Mean contour plots of TKE in the *x–z* plane for nonreacting conditions.

The nondimensional turbulent kinetic energy, TKE/V_b^2, along the centerline of the V-gutter for nonreacting conditions is shown in Fig. 19. The TKE contours show a similar distribution along the span of the V-gutter and result in more intense mixing as the end of the recirculation zone is approached. The line in Fig. 19 represents the height of the *x–y* measurement plane discussed in the preceding section and results in the same TKE contour values at nearly the same downstream locations.

Conclusions

The characteristics of the flowfield around a V-gutter bluff body in both nonreacting and reacting conditions has been determined. This study used an upstream preburner to accurately simulate the flow environment encountered within a jet engine afterburner. The incoming flow to the V-gutter bluff body was a vitiated mixture with secondary liquid fuel being injected upstream through a fuel spray bar to mimic realistic conditions. PIV was used to capture instantaneous and mean flow structures formed in the wake region of a three-dimensional bluff body. In addition to the flow structures, the mean velocity components, mean out-of-plane vorticity, and the turbulent kinetic energy have been compared for the nonreacting and reacting test cases. The results of this study show significant differences between the nonreacting and reacting flowfield. The nonreacting case results in asymmetric shedding of large-scale vortices from the V-gutter edges, whereas the reacting case results in a combination of both symmetric and asymmetric shedding of smaller scale vortical structures that are more elongated and are confined within the shear layers. A comparison of the mean velocity components shows that the reacting case results in a larger region of reversed flow, experiences an acceleration of the freestream flow due to combustion, and results in a slower dissipation of the wake region. For both the nonreacting and reacting case, the shear layer created around the recirculation zone is depicted by the concentration of negative and positive vorticity contours that originate from opposite edges of the V-gutter. In both cases, the vorticity distribution is initially closely spaced and spreads out with downstream distance as it loses strength. The turbulent kinetic energy gives insight into the vortical structures and the mixing processes involved in complex dynamic flows. For the nonreacting case, the mean TKE contours represent the path of the asymmetric large-scale vortical structures being shed from V-gutter edges and convected downstream while moving inward toward the V-gutter centerline. These large-scale structures promote intense mixing between the freestream fluid and the recirculating flow in the near-wake region of the bluff body. For the reacting case, the mean TKE contours are mainly located within the shear layer showing that the roll-up and shedding of the elongated smaller scale vortices are mainly occurring within the shear layer where the chemical reaction takes place. The vortex shedding within the shear layer promotes intense mixing between the fresh freestream mixture and the hot products of the recirculation zone as they are convected downstream.

Acknowledgments

We thank Randy Lewis, Wayne Oliver, and Frank Bachman of General Electric Aircraft Engines, Cincinnati, Ohio, for providing funding and technical assistance with this research study. We also thank Irene Ibrahim for assistance in experimental setup and testing.

References

[1] Longwell, J. P., "Flame Stabilization by Bluff Bodies and Turbulent Flames in Ducts," *Fourth Symposium on Combustion*, Williams and Wilkins, Baltimore, MD, 1953.

[2] Zukoski, E. E., and Marble, F. E., "Role of Wake Transition in the Process of Flame Stabilization on Bluff Bodies," *Combustion Researches and Review*,AGARD, Butterworths, London, 1955, pp. 167–180.

[3] Williams, F. A., "Flame Stabilization of Premixed Turbulent Gases,"

Applied Mechanics Surveys, Spartan, Washington, D.C., 1966, pp. 1157–1170.

[4] Longwell, J. P., "Flame Stabilization and Flame Propagation in Ramjet Combustors," *Combustion Researches and Reviews*, AGARD, Butterworths, London, 1955, pp. 58–71.

[5] Dutta, B. C., Martin, D. G., and Moore, N. W., "Contribution to the Study of Flame Stability in Ducts," *Sixth Symposium International on Combustion*, Yale Univ., Paper 59, 1955.

[6] Sjunnesson, A., Olovsson, S., and Sjoblom, B., "Validation Rig: A Tool for Flame Studies," International Symposium on Air Breathing Engines, Paper 91-7038, 1991.

[7] Sjunnesson, A., Nelsson, C., and Max, E., "LDA Measurements of Velocities and Turbulence in a Bluff Body Stabilized Flame," *Fourth International Conference on Laser Anemometry, Advances and Applications*, Vol. 3, American Society of Mechanical Engineers, 1991, pp. 83–90.

[8] Sjunnesson, A., Henrikson, P., and Lofstrom, C., "CARS Measurements and Visualization of Reacting Flows in a Bluff Body Stabilized Flame," AIAA Paper 92-3650, 1992.

[9] Fujii, S., and Eguchi, K., "Comparison of Cold and Reacting Flows Around a Bluff-Body Flame Stabilizer," *Journal of Fluids Engineering*, Vol. 103, June 1981, pp. 328–334.

[10] Sanquer, S., Bruel, P., and Deshaies, B., "Some Specific Characteristics of Turbulence in the Reactive Wakes of Bluff Bodies," *AIAA Journal*, Vol. 36, No. 6, 1998, pp. 994–1001.

[11] Bakrozis, A., Papailiou, D., and Koutmos, P., "Study of the Turbulent Structure of a Two-Dimensional Diffusion Flame Formed Behind a Slender Bluff Body," *Combustion and Flame*, Vol. 119, No. 3, Nov. 1999, pp. 291–306.

[12] Yue, L., Liu, B., and Yang, M., "Study on the Near-Wake Flow Behind EBMC Flame Holder," *Optical Technology and Image Processing for Fluids and Solids Diagnostics, Proceedings of the SPIE*, Vol. 5058, 2003, pp. 188–198.

[13] Fureby, C., "Large Eddy Simulation of Combustion Instabilities in a Jet Engine Afterburner Model," *Combustion Science and Technology*, Vol. 161, 2000, pp. 213–243.

[14] Giacomazzi, E., Battaglia, V., and Bruno, C., "Coupling of Turbulence and Chemistry in a Premixed Bluff-Body Flame as Studied by LES," *Combustion and Flame*, Vol. 138, No. 4, Sept. 2004, pp. 320–335.

[15] Nillson, P., and Bai, X., "Level-Set Flamelet Library Approach for Premixed Turbulent Combustion," *Experimental Thermal and Fluid Science*, Vol. 21, Nos. 1–3, March 2000, pp. 87–98.

[16] Ji, J., and Gore, J. P., "Flow Structure in Lean Premixed Swirling Combustion," *Proceedings of the Combustion Institute*, Vol. 29, No. 1, 2002, pp. 861–867.

[17] McKenna, S. P., and McGillis, W. R., "Performance of Digital Image Velocimetry Techniques," *Experiments in Fluids*, Vol. 32, No. 1, Jan. 2002, pp. 106–115.

[18] Sung, C. J., Kistler, J. S., Nishioka, M., and Law, C. K., "Further Studies on Effects of Thermophoresis on Seeding Particles in LDV Measurements of Strained Flames," *Combustion and Flame*, Vol. 105, Nos. 1–2, April 1996, pp. 189–201.

[19] Tennekes, H., and Lumley, J. L., *First Course in Turbulence*, MIT Press, Cambridge, MA, 1990.

[20] Bray, K., and Libby, P., "Interaction Effects in Turbulent Premixed Flames," *Physics of Fluids*, Vol. 19, No. 11, 1976, pp. 1687–1701.

[21] Krajnovic, S., and Davidson, L., "Flow Around a Three-Dimensional Bluff Body," *9th International Symposium on Flow Visualization*, Paper No. 177, Heriot-Watt Univ., Edinburgh, Scotland, 2000.

J. Gore
Associate Editor